Aerospace Science and Technology 128 (2022) 107757

Contents lists available at ScienceDirect

Aerospace Science and Technology

www.elsevier.com/locate/aescte

Effect of recess length on flow dynamics in gas-centered liquid-swirl coaxial injectors under supercritical conditions

Liwei Zhang [a,b], Yixing Li [a], Xingjian Wang [a], Vigor Yang [a,*]

[a] School of Aerospace Engineering, Georgia Institute of Technology, Atlanta, GA, USA
[b] Department of Mechanical and Aerospace Engineering, University of Texas at Arlington, Arlington, TX, USA

ARTICLE INFO

Article history:
Received 19 April 2022
Received in revised form 8 July 2022
Accepted 10 July 2022
Available online 16 July 2022
Communicated by Frank K. Lu

ABSTRACT

The flow dynamics in gas-centered, liquid-swirl coaxial injectors at supercritical conditions are comprehensively investigated using the large eddy simulation technique. This class of injectors has been used in many high-performance propulsion and power-generation systems. Gaseous oxygen is axially injected into the center post of the injector at a temperature of 687.7 K, while liquid kerosene is tangentially introduced into the coaxial annulus at a temperature of 492.2 K. The operating pressure of 25.3 MPa substantially exceeds the thermodynamic critical pressures of oxygen and kerosene. Detailed flow structures and mixing layer characteristics are examined, with special attention to the effect of the distance between the end of the center post and the entrance of the taper region, that is, the recess length. Six different cases ranging from no recess to fully recessed are investigated. Various controlling mechanisms of the injector flow dynamics, including recirculating motion near the fuel injection slit, shear-layer instabilities in the recess region, and vortex expansion and merging in the taper region are considered. Dominant frequencies of the axial and azimuthal instability modes are characterized and compared to empirical correlations. Dynamic analyses are conducted for the overall computational domain, as well as individual regions. Among the six cases, only the fully recessed Case 1 exhibits strong pressure oscillations over the entire injector, which are found to be closely related to the longitudinal acoustic oscillations in the center post. In cases with partial or no recess, Case 2 with a long recess achieves the best mixing, and Case 6 with zero recess leads to the worst mixing.

1. Introduction

Injectors are critical components of combustion devices for liquid-fueled propulsion systems [1–4]. By controlling the atomization and mixing of propellants, injectors affect combustion efficiency, dynamic characteristics, and engine life cycle [5,6]. This paper investigates the effects of recess length on the flow dynamics in gas-centered liquid-swirl coaxial (GCLSC) injectors, as shown schematically in Fig. 1. The recess length L_r is defined as the distance between the end of the center tube (known as the GOX post) and the entrance of the taper region. High-temperature gaseous oxygen (GOX) is axially injected into the GOX post, and liquid kerosene is tangentially delivered into the outer annulus. This type of injector design has been widely adopted in the main combustion chambers of many oxidizer-rich staged-combustion cycle engines, such as NK-33, RD-170 and RD-180 [7–11].

Experimental and analytical studies on GCLSC injectors are mostly conducted at low pressures. At atmospheric pressure, interactions between the liquid sheet and gas flow within the injector induce corrugations on the surface of the liquid sheet, and liquid droplets form. After discharge from the injector, the liquid sheet further interacts with the ambient gas and undergoes a series of breakup and atomization processes [12]. Schumaker et al. [13,14] performed cold-flow experiments of nitrogen and water at atmospheric pressure. The momentum flux ratio, recess length, and swirl strength were found to be the main parameters determining the overall spray characteristics of GCLSC injectors. Kulkarni et al. [15] studied the liquid-gas interaction and breakup behavior at atmospheric condition using air and water as working fluids. Various liquid-gas interaction mechanisms were identified over a range of liquid sheet inertia. The breakup length decreases with increasing jet Reynolds number. Park et al. [16] studied the influences of geometric parameters on both spray characteristics, such as film thickness and spray angle, and breakup behavior of GCLSC injectors at atmospheric pressure. Matas et al. [17] explored the flow dynamics of GCLSC injectors using water and air. The surface instability was attributed to viscous shear stress caused by

* Corresponding author.
E-mail address: vigor.yang@aerospace.gatech.edu (V. Yang).

https://doi.org/10.1016/j.ast.2022.107757

the differences of velocity and viscosity across the interface. The frequencies of flow oscillations increase with gas velocity and do not depend on the initial swirl number.

The above studies provide useful information about liquid spray dynamics at subcritical pressures. Flow behaviors in the supercritical region, however, are significantly different [18]. At supercritical conditions, the lack of surface tension eliminates the formation of droplets. Moreover, thermodynamic nonidealities and transport anomalies fundamentally change fluid behaviors, especially in the transcritical region. These characteristics must be taken into account in the treatment of supercritical fluid flows. A few studies have recently been conducted at elevated pressures. Kim et al. [19] carried out cold-flow experiments at both 0.1 MPa and 5.9 MPa. The influences of recess length and momentum flux ratio on the spray pattern of GCLSC injectors were examined. Experimental studies on reacting flows in the pressure range of 4-8 MPa were also performed [20,21], focusing on the spectral content of flow evolution and mixing/combustion efficiencies. Such pressure conditions, however, are considerably lower than the nominal combustion chamber pressures in staged combustion rocket engines [7–10,22]. For example, the RD-170 main combustion chamber operates at 25.3 MPa, and the preburner at 55 MPa [7,8,22]. A comprehensive study of flow dynamics of GCLSC at supercritical conditions typical of practical rocket engine operation is needed.

It is well established that the recess of the center tube in a coaxial injector improves the mixing of gas and liquid streams [23]. Ahn et al. [24] studied the effect of recess length on the mixing and combustion dynamics in a combustor with 19 bi-swirl injectors over a pressure range of 4.2-5.4 MPa. For each injector, liquid oxygen (LOX) and kerosene were injected tangentially into the center tube and coaxial outer annulus, respectively. As recess length increases, the mixing type was found to shift from an external to an internal mode, thereby improving the mixing and combustion efficiencies. The same authors then explored the effect of recess length on discharge coefficient [25]. Results indicated that longer recess length moderately reduces the discharge coefficient. Wang et al. [26,27] simulated flow evolution of recessed and non-recessed LOX/kerosene bi-swirl injectors at supercritical conditions. Both non-reacting and reacting cases were considered. The work further confirmed the enhancement of propellant interaction in the recess region. Various underlying mechanisms and processes were investigated at scales sufficient to identify the key flow physics. On the theoretical side, Juniper and Candel [28] studied the stability of a coaxial injector with water flow from the center tube and high-velocity air flow through the outer annulus at atmospheric pressure. A two-dimensional ducted compound flow model was developed, indicating that the recessed coaxial injector has a much larger region of absolutely instability than its non-recessed counterpart. The positive influence of recess region on mixing efficiency was qualitatively corroborated, although the optimum recess length was not identified.

Recently, with advances in experimental and computational capabilities, several comprehensive studies have been performed on GCLSC injectors at supercritical conditions. Balance et al. [29] conducted optical diagnostic experiments on the combustion dynamics of a GCLSC injector in the pressure range of 2-16.5 MPa using GOX and liquid kerosene as propellants. The flame stabilization mechanism and near-field flame structure at high pressures were found to be significantly different from those at low pressures. Yang and colleagues [30–32] conducted comprehensive numerical investigations into the flow and combustion physics of GCLSC injectors at conditions mimicking the operation of the main combustion chamber of a flight staged-combustion cycle engine (i.e., RD-170 engine). The present work complements these earlier studies [30–32], for the first time to comprehensively identify and analyze dynamic characteristics in GCLSC injectors, and also examines the effect of recess length on the injector flow dynamics under supercritical conditions. The flow physics are analyzed in detail and key parameters dictating flow evolution are identified.

This paper is organized as follows. In Section 2, the theoretical and numerical framework is briefly introduced. In Section 3, the injector geometry and flow conditions are described. In Section 4, detailed discussions of flow and mixing characteristics are provided, with special attention given to the influence of recess length. Conclusions are summarized in Section 5.

2. Theoretical and numerical framework

The basis of the present work is the integrated theoretical and numerical framework detailed in [18,33–35]. The model is capable of treating general fluid dynamics over a wide range of fluid thermodynamic states, from ideal gas to supercritical fluid. The formulation treats the Favre-averaged conservation equations of mass, momentum, energy, and species concentrations. Turbulence closure is achieved by the large eddy simulation technique, with subgrid-scale motions modeled using a compressible-flow version of the Smagorinsky model [36]. Thermodynamic properties, including density, enthalpy, and specific heat, are evaluated over a broad range of temperature and pressure using fundamental thermodynamics theories and a modified Soave-Redlich-Kwong equation of state. Transport properties, including thermal conductivity and viscosity, are determined using extended corresponding-state principles. Mass diffusivity is estimated based on the Takahashi method calibrated for high-pressure conditions. A comprehensive description of property evaluation schemes is given in [18]. A three-component surrogate model consisting of n-decane, n-propylbenzene, and n-propylcyclohexane (74/15/11% by mole fraction) is used to calculate physicochemical properties of kerosene [37].

The numerical framework is established to be self-consistent and robust by means of a pre-conditioning scheme and a unified treatment of general-fluid thermodynamics [34]. It employs a density-based finite-volume methodology along with a dual-time-stepping integration technique [38,39]. Temporal discretization is achieved using a second-order backward difference scheme, and the inner loop pseudo-time term is integrated with a four-step Runge-Kutta scheme. Spatial discretization is obtained by a fourth-order central difference scheme in generalized coordinates. A fourth-order matrix dissipation is employed to ensure numerical stability with a minimal contamination of the solution. A multi-block domain decomposition technique with message passing interfaces at domain boundaries is used to facilitate parallel programming and optimize computational speed.

3. Injector geometry and flow conditions

3.1. Geometric configurations

Fig. 1 shows schematically the GCLSC injector under consideration, mimicking the main chamber injector of the staged-combustion rocket engine RD-170/180 [8–11,22]. The injector is composed of four parts: a center cylindrical tube, coaxial annular fuel passage, recess region, and a taper region. High-temperature GOX is introduced axially into the GOX post, and kerosene is tangentially injected into the coaxial annulus at a tangential angle $\theta = 63.4^\circ$. In the original injector design, there are a total of 12 fuel ports distributed in two arrays and each has a diameter, D_i, of 1.2 mm. In the present study, these fuel ports are simplified by a single circular slit and the slit width is determined as $\delta = 12\pi\,(0.5D_i)^2/2\pi R_f \cos\theta = 0.69$ mm to ensure the same mass and momentum flow rates as those in the original design [30]. The fuel injection velocity components in the axial, azimuthal, and

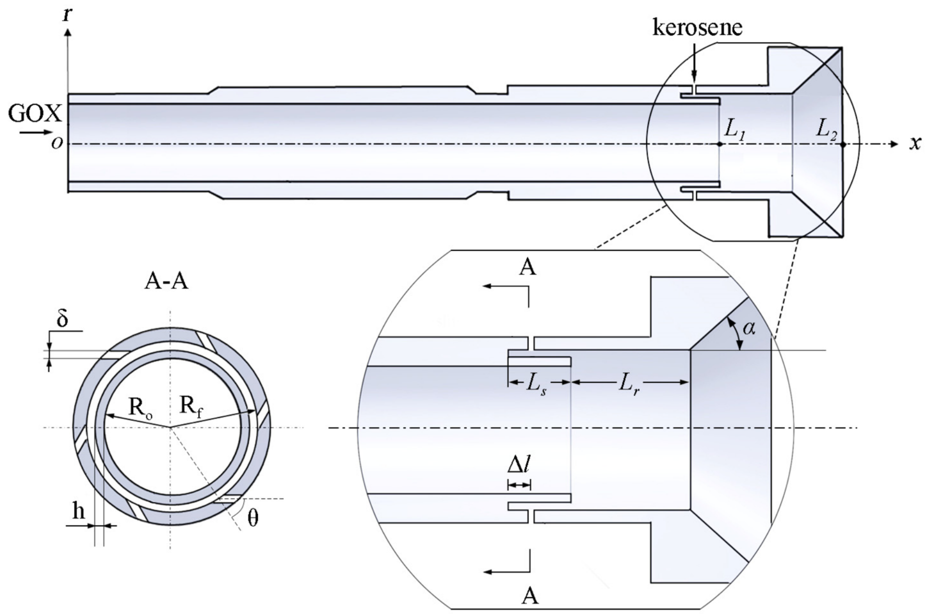

Fig. 1. Schematic of gas-centered liquid-swirl coaxial (GCLSC) injector.

Table 1
Geometric parameters of baseline injector.

δ, mm	h, mm	R_o, mm	R_f, mm	L_1, mm	L_2, mm	Δl, mm	α
0.69	0.7	5.6	7.0	93.0	113.1	2.0	42°

Table 2
Injection conditions for fuel and oxidizer.

	Oxidizer	Fuel
Fluid	GOX	Kerosene
Mass flow rate, kg/s	1.33	0.48
Static pressure, MPa	25.3	25.3
Temperature, K	687.7	492.2
Density, kg/m^3	131.4	640.8
Momentum flux, 10^6 kg/m s^{-2}	1.367	0.385

radial directions are $u_x = 0$, $u_\theta = u_{in} \sin\theta$, and $u_r = u_{in} \cos\theta$, respectively, where $u_{in} = \dot{m}/(\rho A_{in})$. Mixing of GOX and kerosene begins in the recess region and continues downstream in the taper region. Table 1 and Table 2 list the geometric parameters and operating conditions of the injector.

In the present work, six different recess lengths (L_r) are considered in the range of 0-16 mm. The distance from the headend of the fuel annulus to the entrance of the taper region is fixed at 16 mm. The length of the annulus inner surface (shielding length, L_s) thus changes according to the variation of the recess length L_r. Table 3 lists the lengths of recess and shielding for all cases. (The recess length decreases with increasing case number.) Case 3, with a recess length of 5.5 mm, is considered as the baseline, while Case 1 is fully recessed, and Case 6 has no recess. Other geometric parameters remain identical as listed in Table 1.

The injector operating pressure is 25.3 MPa, identical to the main combustor pressure of the RD-170/180 engines. Note that the critical pressure and temperature are 5.1 MPa and 154.8 K for oxygen and 1.8 MPa and 658.2 K for dodecane, respectively. Table 2 lists the injection conditions for fuel and oxidizer streams. The densities of GOX and kerosene at their entrances are 131.4 and 640.8 kg/m^3, respectively, and the axial velocity of the incoming GOX stream is 102 m/s. The reference entrance velocity of kerosene, U_f, needs to be evaluated carefully. For Case 1, without shielding, the kerosene radially penetrates the axial GOX stream, and U_f is taken as the radial velocity component at the inlet, 24.5 m/s. For other cases with shielding, kerosene flows axially at the point of mixing, and U_f is most appropriately represented by the axial velocity in the coaxial outer annulus, 26.6 m/s. The momentum flux between the GOX and fuel stream, defined as $\rho_o U_o^2/\rho_f U_f^2$, is thus obtained as 3.5 for Case 1 of a transverse kerosene jet into a GOX crossflow, and 3.0 for Cases 2-6 of co-flowing kerosene and GOX streams. The Reynolds numbers based on the axial velocities are 1.89×10^6 and 4.14×10^4 for the GOX and kerosene flows, respectively, taking the center post diameter and outer annulus width as the characteristic lengths.

3.2. Computational implementation

The computational domain is comprised of the injector (shown in Fig. 1) and its downstream region, which spans 90 and 158 mm in the radial and axial directions, respectively. The present study considers a three-degree cylindrical sector of the three-dimensional domain, with periodic boundary conditions in the azimuthal direction. It is known this axisymmetric simulation has the limitations of neglecting flow dynamics in the azimuthal direction and missing some of the vortex-stretching mechanism responsible for turbulent energy transfer from large to small eddies. Nevertheless, previous studies have shown this method is able to capture many unique features of supercritical flows, including density stratification, interfacial instability, and real-fluid effects. In a recent study comparing simulations based on a cylindrical sector and a three-dimensional domain, close agreement was observed in most of the axial dynamics [32]. Given that it is computationally prohibitive to perform three-dimensional computations, only a cylindrical sector is simulated in the present work focusing on the influence of recess length over a series of cases at a manageable turnaround time.

At the GOX and kerosene inlets, boundary conditions are treated based on the method of characteristics [40], and accom-

Table 3
Lengths of recess and shielding for six cases.

Case	1 no shielding	2	3 baseline	4	5	6 fully shielded
L_s, mm	0.0	3.0	5.5	9.0	12.5	16.0
L_r, mm	16.0	13.0	10.5	7.0	3.5	0.0

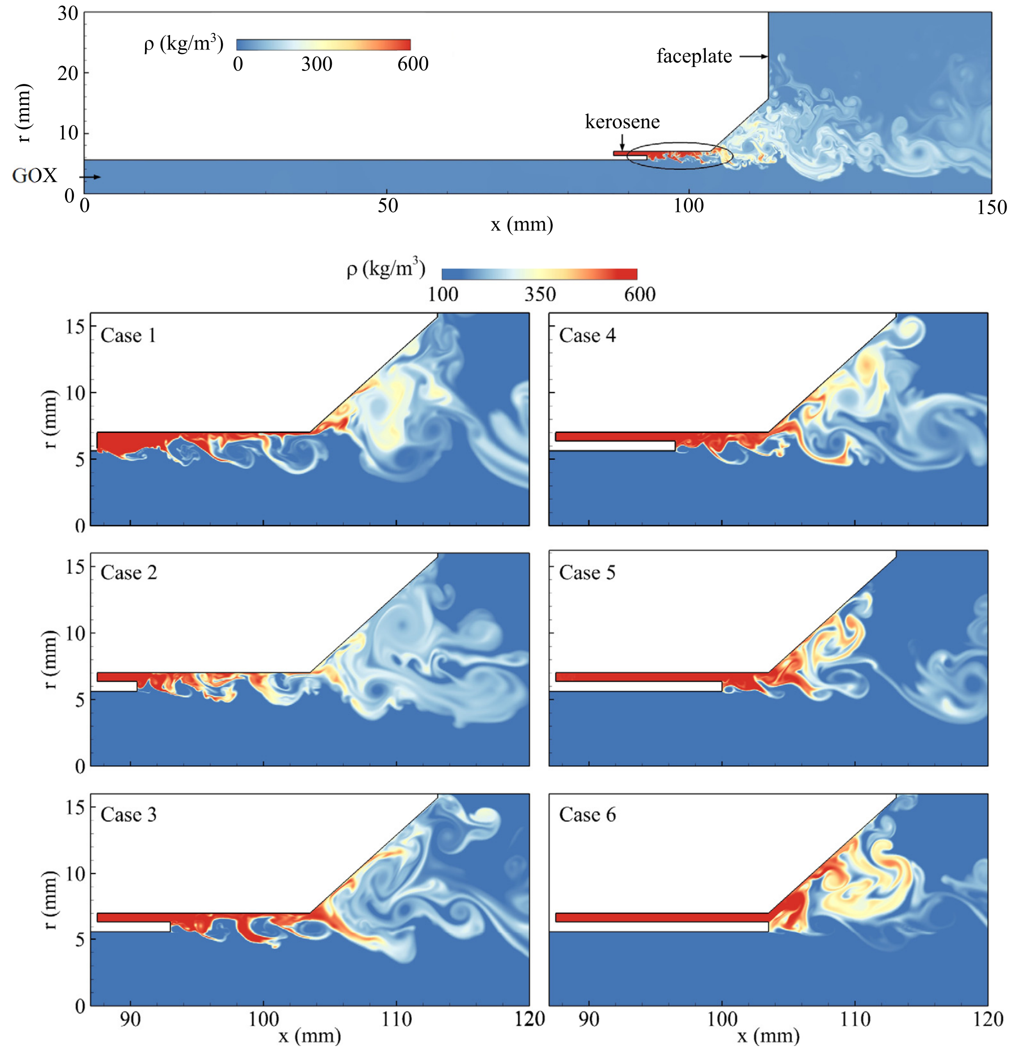

Fig. 2. Snapshots of density field (global view for the baseline case and zoom-in views for all six cases).

modate appropriate acoustic and hydrodynamic flow characteristics without unphysical reflection. At the downstream boundary, a sponge-layer treatment [41] is implemented in both the axial and circumferential directions. No-slip and adiabatic conditions are applied at the injector walls. White noise with 5% intensity is applied to the inlet velocities of both propellant streams.

4. Results and discussion

The theoretical/numerical framework has been validated against multiple supercritical fluid flow problems, and a grid independence study has been carried out for the baseline case [30]. The intermediate level 2 grid is selected for subsequent calculations in the present study, as a tradeoff between computational efficiency and accuracy. At this level, the grid sizes are 5 μm near the injector wall and 10 μm near the GOX post tip surface in the radial direction, comparable to the Taylor scale inside the fuel annulus. Table 4 summarizes the detail of the selected grid.

4.1. Flow structures

Fig. 2 show snapshots of the density fields for the baseline case in a global view and for all six cases in zoom-in views of the recess region, respectively. The origin of coordinates is located at the center of the GOX inlet. High-speed, low-density GOX flows through the center post, while low-speed, high-density kerosene is delivered tangentially into the fuel passage through the injection slit. The kerosene stream forms a thin film and travels along the injector wall in the recess region due to swirl-induced centrifugal force. The GOX stream, with a higher momentum flux, entrains kerosene, leading to the formation of fuel ligaments that penetrate the GOX flow. The fuel ligaments continue to disintegrate and mix with GOX while travelling downstream. A previous study has shown that the density difference in the incoming kerosene and GOX streams has little contribution on the early mixing layer development herein [30]. Differences in the fuel shielding and the kerosene velocity profile entering the GOX flow, however, affect the density distri-

Table 4
Grid numbers of each region for the baseline case.

	GOX post	fuel passage	mixing cup	downstream
grid number in x-coordinate	448	112	320	320
grid number in r-coordinate	128	48	224	320
total cells, 10^4	5.73	0.54	7.17	10.24

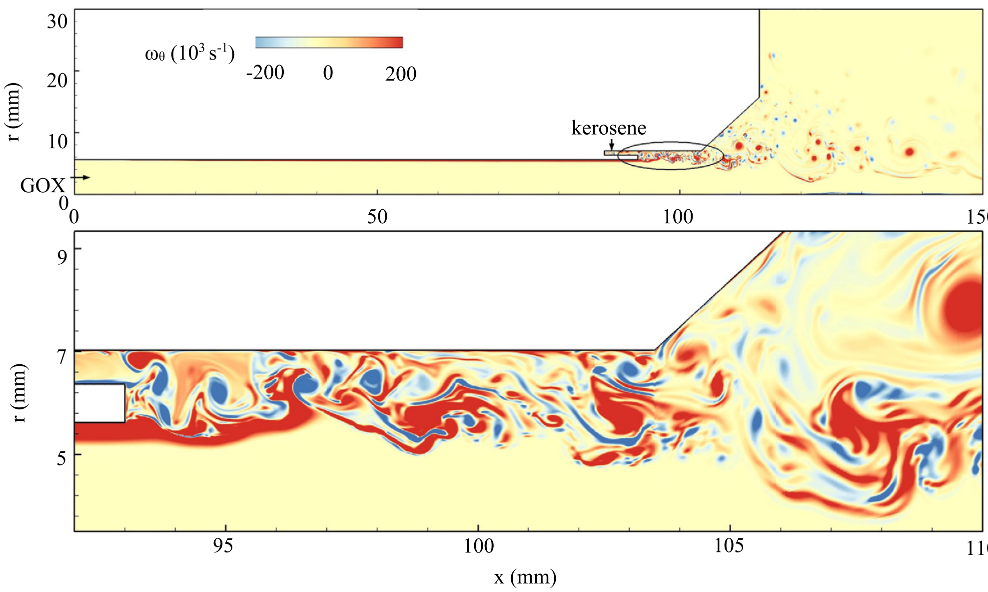

Fig. 3. Snapshots of azimuthal vorticity fields (global and zoom-in views for the baseline case).

bution in the recess region. In Case 1, without fuel shielding, the swirling kerosene is injected transversely into the GOX crossflow, and immediately penetrates towards the post center, inducing a wider kerosene dispersion and stronger macromixing in the recess region. In Cases 2-5, with partial fuel shielding, kerosene enters the recess region axially and the mixing layer of the coflow kerosene and GOX only starts to form after the recirculation zone behind the post rim. In Case 6, with a full fuel shielding, kerosene is injected into the diverging section of the injector. While the taper region facilitates the radial expansion and dispersion of both flows, its influence on the mixing of the coflow kerosene and GOX is yet to be evaluated. According to classic hydrodynamics theories [5,6], the spreading angle of swirling kerosene is estimated to be around 60°, larger than the taper angle of 42°, so the kerosene film thus attaches to the taper surface. The mass and momentum transfer with the GOX stream, however, result in reduced radial velocity and increased axial velocity of kerosene as it flows downstream. Therefore, the attachment of kerosene to the taper surface becomes weaker and disappears in all cases after $x = 110$ mm.

Since Case 1 without fuel shielding has been discussed in an early work [30], the current paper focuses on the cases with a finite fuel shielding and examine the length effects. To illustrate the dynamic flow features, Fig. 3 show snapshots of the azimuthal vorticity fields ($\omega_\theta = \partial u_r/\partial x - \partial u_x/\partial r$) for the baseline case in a global view and a zoom-in view in the recess and taper regions. In the wake of the post rim, sudden flow expansions induce the radial motions, inward for the kerosene and outward for the GOX, generating negative vorticities in the kerosene and positive vorticities in the GOX streams, respectively. These additional vorticities intensify the dynamic characteristics of the early-stage mixing [30]. In the latter recess region, further vorticities, mostly positive in the azimuthal component, are produced due to the baroclinic effect from the misalignment of density and pressure gradients in the mixing layer [32]. Depending on the recess length, the mixing and vorticity fields undergo different development before entering the taper region. As opposed to the two-way expansion near the post rim, the mixture flow expands radially outward in the taper region, leading to an increase in the radial velocity and a decrease in the axial velocity. Hence, positive azimuthal vorticities are noticeably augmented, accompanying by the complicated flow structures in the further downstream. The flowfield in each section of the injector is presented in detail as follows.

4.1.1. Fuel annulus

Fig. 4 shows the temporal evolution of the azimuthal vorticity field overlaid by streamlines, near the injection slit in the fuel annulus within one cycle of flow oscillation for the baseline case. The time interval, Δt, between plots is 0.04 ms. Shear layers form on both sides of the injected fuel stream. They roll up and result in the development of recirculation bubbles, indicated by green circles in the top plot. At time t_o, the recirculation bubble in the upstream of the injection slit starts to evolve. It expands in the radial direction and eventually separates into two bubbles at $t_o + 0.16$ ms. The inner one travels downstream, while the outer one continues to grow and repeats the same process. The shedding frequency is 5.6 kHz. Immediately downstream of the injection slit, similar vortex dynamics are observed. The counter-clockwise recirculation bubble grows and horizontally splits into two bubbles; the one in the upstream region continues to evolve while the other convects downstream. The shedding frequency is estimated to be 13 kHz. Both frequencies are related to the initial kerosene injection scheme, and hence, are approximately the same for all the cases with a finite shielding in the present study.

As kerosene moves along the fuel passage, its velocity distribution changes over the distance. Fig. 5 shows the radial distribution of time-mean axial and azimuthal velocities at end of the GOX post. For Case 2, the kerosene flow is not fully developed in the annulus. Flow reversal is observed near the upper wall. The axial velocity of the kerosene flow in Case 2 is larger than those in Cases 3-5. Moreover, the radial location of the maximum axial ve-

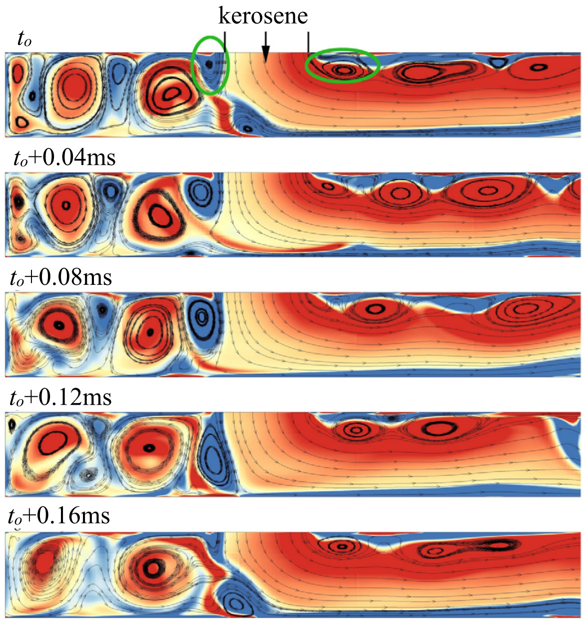

Fig. 4. Temporal evolution of azimuthal vorticity overlaid by streamlines near the fuel injection slit in the fuel annulus for the baseline case. (For interpretation of the colors in the figure(s), the reader is referred to the web version of this article.)

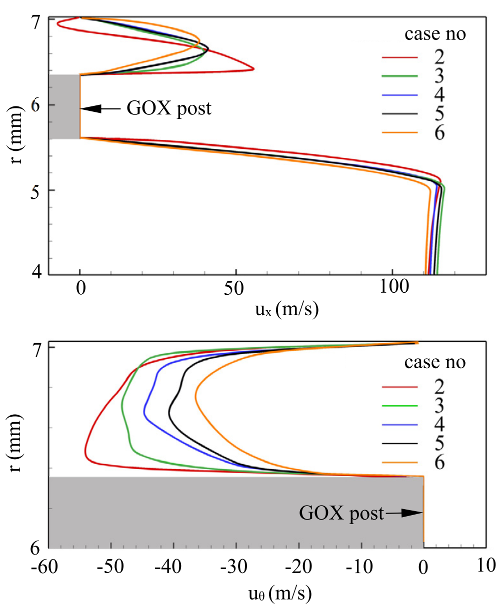

Fig. 5. Radial distribution of time-mean axial and azimuthal velocities at the end of GOX post for Cases 2-6.

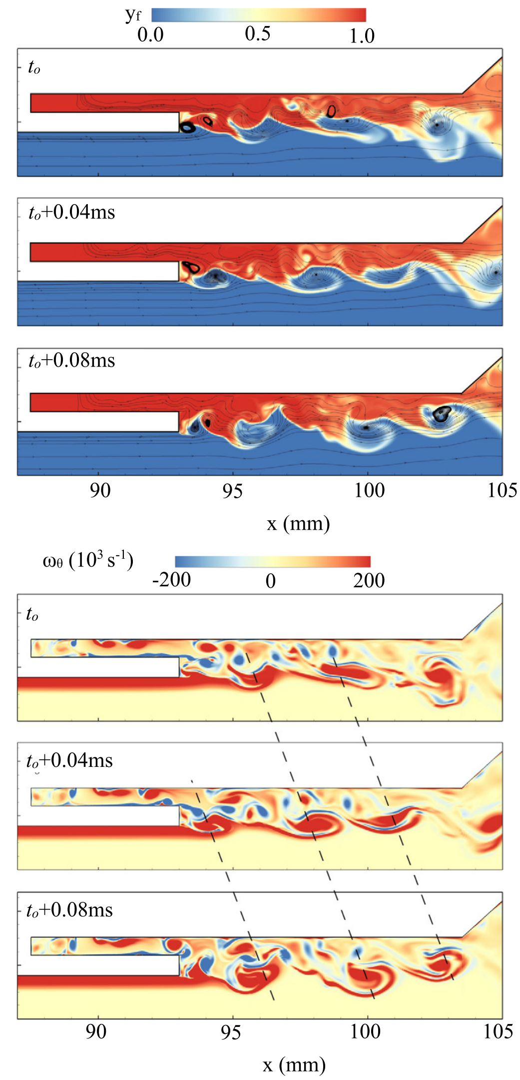

Fig. 6. Temporal evolution of a) fuel mass fraction overlaid by streamlines, and b) azimuthal vorticity in the recess region for the baseline case.

locity of the fuel stream is closer to the GOX stream, resulting in a smaller momentum thickness δ.

4.1.2. Recess region

The shielding collar rim downstream of the fuel annulus acts as a splitter plate between the fuel and oxidizer flows. It allows for the development and shedding of vortices generated from both the GOX and kerosene streams. Fig. 6 shows the temporal evolutions of fuel mass fraction, overlaid by streamlines and azimuthal vorticity in the recess region for the baseline case. The shear layer instability induced by the velocity gradient is clearly observed. At time t_o, immediately downstream of the shielding collar rim, the GOX stream rolls up and forms a large-scale counterclockwise rotating vortex. After 0.04 ms, while the vortex convects downstream, it detaches from the rim and entrains the liquid kerosene stream into the GOX flow. At $t_o + 0.08$ ms, the vortex further grows and facilitates the liquid entrainment and subsequent mixing between the GOX and kerosene. The propagation speed of the large-scale vortices is approximately $\overline{u} = 60$ m/s, the average velocity of the GOX and kerosene flows. The distance between neighboring vortices is around $\Delta s = 4$ mm. The corresponding frequency is estimated to be on the order of $f = \overline{u}/\Delta s = 15$ kHz.

Fig. 7a shows the radial distributions of time-mean axial velocity at different axial locations for the baseline case, where L_p is the distance from the fuel collar rim. No-slip conditions are imposed at the injector wall and GOX post surface, leading to low velocities adjacent to these surfaces. Immediately downstream of the GOX post ($L_p = 2$ mm or less), the flow close to the injector wall consists mainly of the injected kerosene and the local velocity profile is parabolic, while the flow in the center region is primarily made of GOX and has a top-hat velocity profile. Mixing of the kerosene and GOX streams starts in the overlapping region of the two velocity profiles. As the flow moves downstream ($L_p =$ 4-10 mm), the peak velocity in the near-wall kerosene stream decreases due to viscous wall friction. Mixing between kerosene and GOX, as well as momentum exchange, reduces the maximum axial velocity in the center region, a phenomenon typically observed in the development of a confined jet [42]. Fig. 7b shows the radial dis-

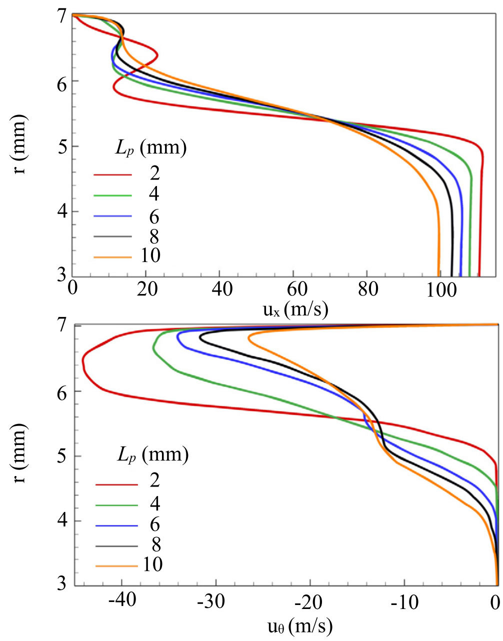

Fig. 7. Radial distributions of time-mean (a) axial and (b) azimuthal velocities at different axial positions in the recess region for the baseline case (L_P = distance from the end of GOX post).

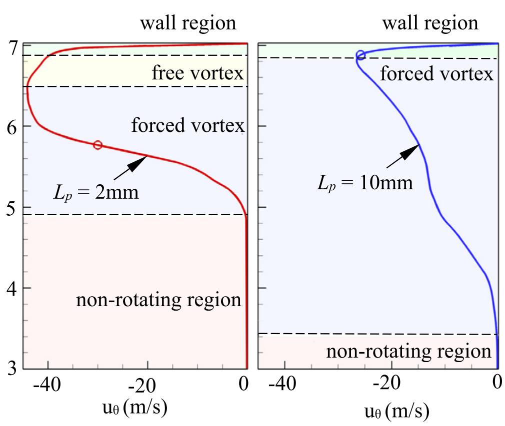

Fig. 8. Flow structures in recess region for the baseline case at $L_p = 2$ and 10 mm (L_p = distance from the end of GOX post).

tributions of time-mean azimuthal velocity at the corresponding axial locations in Fig. 7a. Similar to the axial velocity, the azimuthal velocity exhibits an almost parabolic profile at $L_p = 2$ mm, with some deviation in the wake of the GOX post due to the mixing of kerosene and GOX. The parabolic shape gradually disappears at $L_p = 4$-10 mm, as the mixing between kerosene and GOX continues downstream.

Fig. 8 shows close-up views of azimuthal velocity profiles at $L_p = 2$ and 10 mm. The flowfield at $L_p = 2$ mm can be radially divided into four regimes: the non-rotating, forced-vortex, free-vortex, and wall regions. The incoming GOX stream has a high axial velocity of $u_x \approx 110$ m/s, creating a non-rotating core in the center region ($0 < r < 4.9$ mm), where the azimuthal velocity remains unchanged, i.e., $u_\theta \approx 0$. As the radial distance from the centerline further increases (4.9 mm $< r <$ 6.5 mm), the region is still primarily filled with GOX and has an increasing azimuthal velocity, i.e., $u_\theta \propto r$, indicating a forced-vortex region and a rigid-body rotation of GOX therein. Further away from the centerline (6.5 mm $< r <$ 6.8 mm), the kerosene film has a constant azimuthal momentum, i.e., $u_\theta \propto 1/r$, suggesting an irrotational free-

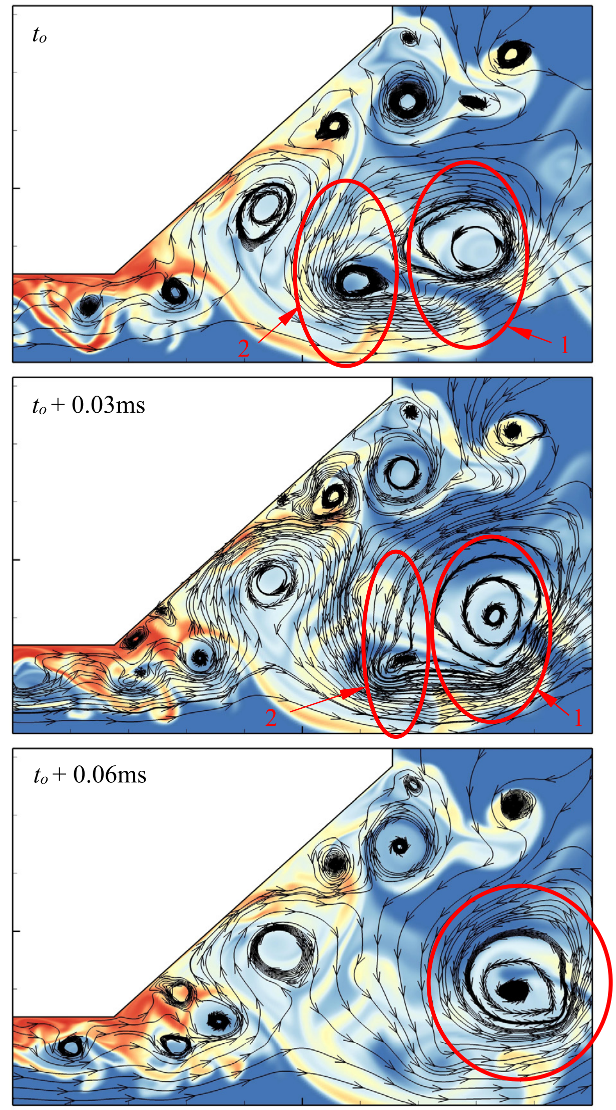

Fig. 9. Temporal evolution of fuel mass fraction and streamlines in taper region for the baseline case.

vortex region. Near the wall (6.8 mm $< r <$ 7.0 mm), a boundary layer is developed, and the velocity diminishes rapidly to zero. In the downstream region at $L_p = 10$ mm, mixing and momentum transfers between kerosene and GOX result in an expanded forced-vortex region, a vanished free-vortex region, and a diminished non-rotating core. Under supercritical conditions, the spatial transition from liquid to gas spans a finite region. The gas-liquid interface, defined (for the purposes of discussion) at the location of the maximum density gradient normal to the interface [43], is marked with small circles in Fig. 8. In the initial mixing zone ($L_p = 2$ mm), the gas-liquid interface lies in the forced-vortex region. The interface moves toward the wall in the downstream region ($L_p = 10$ mm), due to the radial expansion of the GOX flow.

4.1.3. Taper region

As the flow expands in the diverging taper region, both the axial and azimuthal velocities outside the center region ($r > 3.5$ mm) decrease in magnitude, causing the pressure to recover in the downstream region. The resultant axial positive pressure gradient leads to a large clockwise recirculating flow near the taper wall. A similar phenomenon, commonly known as vortex breakdown, is observed in the flowfields of swirl injectors [44,45,43,46,47], where a central recirculation zone is developed. For GCLSC injectors, the

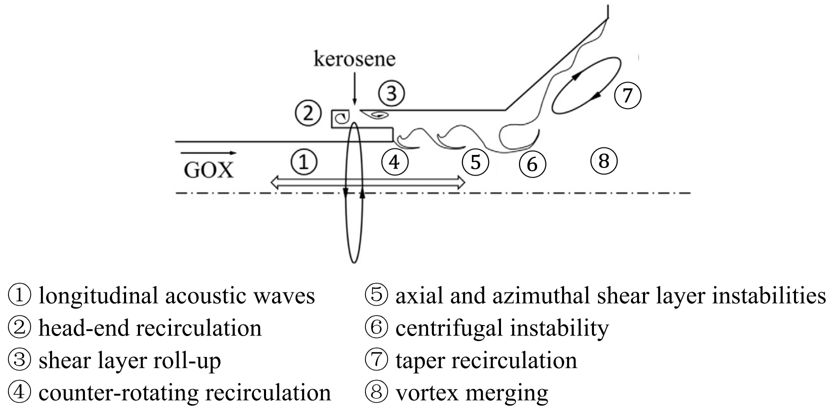

Fig. 10. Flow dynamics in the GCLSC injector with a finite fuel shielding.

recirculating flow is located between the outer kerosene and central GOX streams.

Fig. 9 shows the temporal evolution of fuel mass fraction and streamlines in the taper region for the baseline case. Small eddies remain stationary near the wall, while large-scale vortices in the recirculation region undergo complex interactions, including propagation, disintegration and merging. At time t_o, two vortices, denoted as 1 and 2, are convected downstream from the recess region. Influenced by centrifugal force, Vortex 1 travels radially outward, but decelerated by the low-speed center stream. For Vortex 2, the centrifugal force is balanced under the influence of Vortex 1. It flows axially downstream. Merging of the two vortices starts at $t_o + 0.03$ ms and completes at $t_o + 0.06$ ms, due to the difference in the axial velocity of the two vortices.

4.2. Dynamic analyses of the flowfield

Fig. 10 summarizes the salient flow features in a GCLSC injector with a finite fuel shielding. The flowfield in the fuel annulus features shear layer roll-up and vortex shedding near the injection slit. Two counter-rotating recirculation bubbles form behind the GOX post rim. As the GOX and kerosene mix in the recess region, Kelvin-Helmholtz instabilities in both axial and azimuthal directions become prominent, due to strong velocity gradients between the two flows. Strongly influenced by shear layer instability, centrifugal instability further induces the oscillation of the liquid kerosene film. Further downstream, area expansion, combined with centrifugal instability, gives rise to large-scale vortices near the taper wall. In the center of the taper, vortices undergo a process of expansion, interaction, and merging. To obtain an in-depth understanding of flow characteristics, dynamic analyses of the flowfield have been performed using the power spectral density (PSD) and the proper orthogonal decomposition (POD) methods.

4.2.1. Power-spectral-density analysis

The flowfield is extensively probed at each section of the injector. Probes placed in the GOX post have been presented in an early work [30] and are omitted here. All probes from Cases 1 and 4 (used as a sample case with fuel shielding) show almost identical contents that have the peak frequency around 2.4 kHz, indicating the dominance of the longitudinal acoustic oscillations in the GOX post. For Case 1, this dominant frequency persists in the recess and taper regions, except for the probe near the fuel slit, which shows a peak frequency about 13 kHz. The latter frequency is related to the kerosene injection process as discussed in Fig. 4.

For cases 2-6 with fuel shielding, more dominant frequencies are detected in the mixing layers in the recess and taper region. Fig. 11 shows the spectral contents of pressure oscillations for the baseline case. The probe locations are shown in Fig. 11a. In the recess region, two probes are placed near the mixing layer, located on the GOX and fuel sides, respectively. Dominant frequencies of 1.9 kHz, 3.6 kHz, 6.2 - 6.6 kHz and 11 - 13 kHz are observed at both probes. The dominant frequency of the Kelvin-Helmholtz instability follows

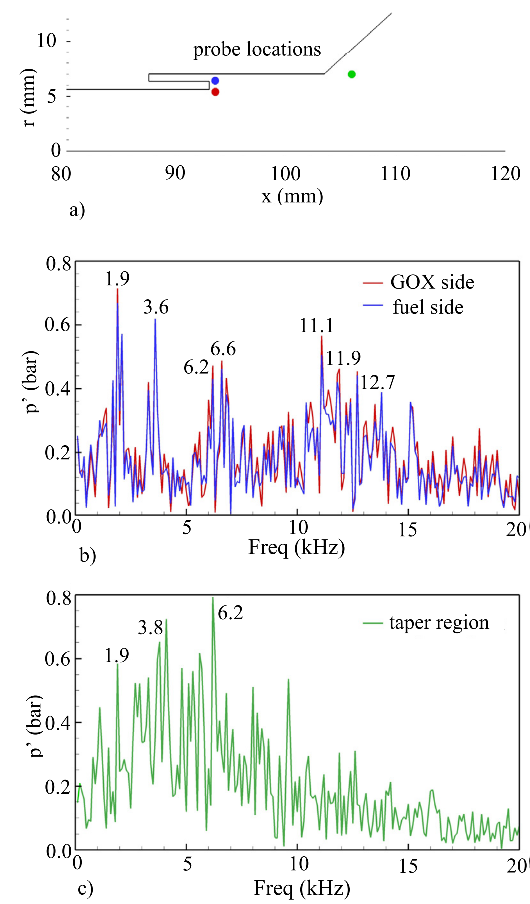

Fig. 11. Power spectral densities of pressure oscillations at three different locations in (b) recess and (c) taper regions for the baseline case.

$$f = St \cdot \overline{u}/\delta \tag{1}$$

where the average velocity $\overline{u} = 1/2 \times (u_1 + u_2)$, with u_1 and u_2 being the axial flow velocities at the two sides of the shear layer. The initial momentum thickness of the shear layer δ is defined as one fourth of the vorticity thickness, $\delta = 1/4 \times (u_1 - u_2)/(du/dy)_{max}$

Table 5
Shear layer instability frequency for Cases 1-6.

Case No	1	2	3	4	5	6
axial (kHz)	13.0	15.6	11.1	10.9	11.8	12.3
azimuthal (kHz)	5.1	5.2	3.6	3.4	3.2	2.8

[48,49]. For the baseline case, the averaged axial velocity $\overline{u}$ is 60 m/s and the estimated δ is approximately 0.25 mm. With $f = 11.1$ kHz, the Strouhal number St becomes 0.046 according to Eq. (1), which falls within the range of 0.044 - 0.048 for the most unstable mode of an unforced planar shear layer in turbulent flows [50]. The frequency of 3.6 kHz is identified as the dominant mode in the azimuthal direction. With $f = 3.6$ kHz and using the azimuthal velocities for u_1 and u_2, the Strouhal number is estimated to be 0.041, also within the empirical range of 0.044 - 0.048. The frequency range of 6.2 - 6.6 kHz, roughly half of 11 - 13 kHz, represents the sub-harmonics of the shear layer instability. It can be attributed to the vortex merging process, which starts in the recess region and becomes prominent in the taper region. Similarly, the 1.9 kHz oscillation corresponds to the sub-harmonics of shear layer instability in the azimuthal direction.

The recess length has a strong impact on the axial velocity of the fuel stream and consequently influences the shear layer instability. Table 5 summarizes the dominant frequencies of the axial and azimuthal modes of the instabilities for different recess lengths. For the axial shear-layer instability, cases 2-5 can be categorized into three groups (Case 2, Case 3-5, Case 6). For Case 2 with a short fuel shielding, the kerosene flow is not fully developed before exposing to the GOX flow; the axial velocity of the fuel stream changes drastically in the recess region and consequently influences the shear layer instability. Since the flow instability f is proportional to u_x/δ, Case 2 has a larger instability frequency. For injectors with a medium recess length (Cases 3-5), the kerosene flow is fully developed in the annulus. The influence of recess length on shear layer instability appears to be fixed. In Case 6, the GOX post extends to the entrance of the taper region. The dominant frequency of the axial shear layer instability increases to 12.3 kHz, as a result of complicated interactions between vortex expansion and geometric variation. On the other hand, frequencies of the azimuthal shear-layer instabilities decrease as the recess length is shortened. This trend can be explained by the time-mean azimuthal velocities at the shielding collar rim in Fig. 5b and the empirical correlation $f \sim u_\theta/\delta$.

In the taper region, one probe is placed in the kerosene plume. Fig. 11c shows the frequency content of the power spectral density of the pressure oscillation. The dominant frequency is found to be 6.2 kHz. It is attributed to the vortex merging process, as it is approximately one half of the shear layer instability frequency in the axial direction in the recess region. Other dominant modes are associated with the recess region.

4.2.2. Proper-orthogonal-decomposition analysis

To further elaborate on the flow dynamics, POD of fluctuating pressure is applied to different regions of the injector. Fig. 12 shows the distributions of pressure oscillations inside the GOX post and in the downstream of the taper region for the baseline case. Only the first four POD modes are shown. In Fig. 12a, inside the GOX post, all modes are correlated to longitudinal modes, and higher POD modes represent higher longitudinal modes. Although not shown here, POD analyses were also conducted in the recess region, and the results show that the prominent longitudinal acoustic modes are stronger than the hydrodynamic instabilities in the mixing layers. Nevertheless, the pressure oscillations in these regions (shown over the range of $-8 < p' < 8$ bar in Fig. 12a) are much smaller than those in the downstream of the taper region

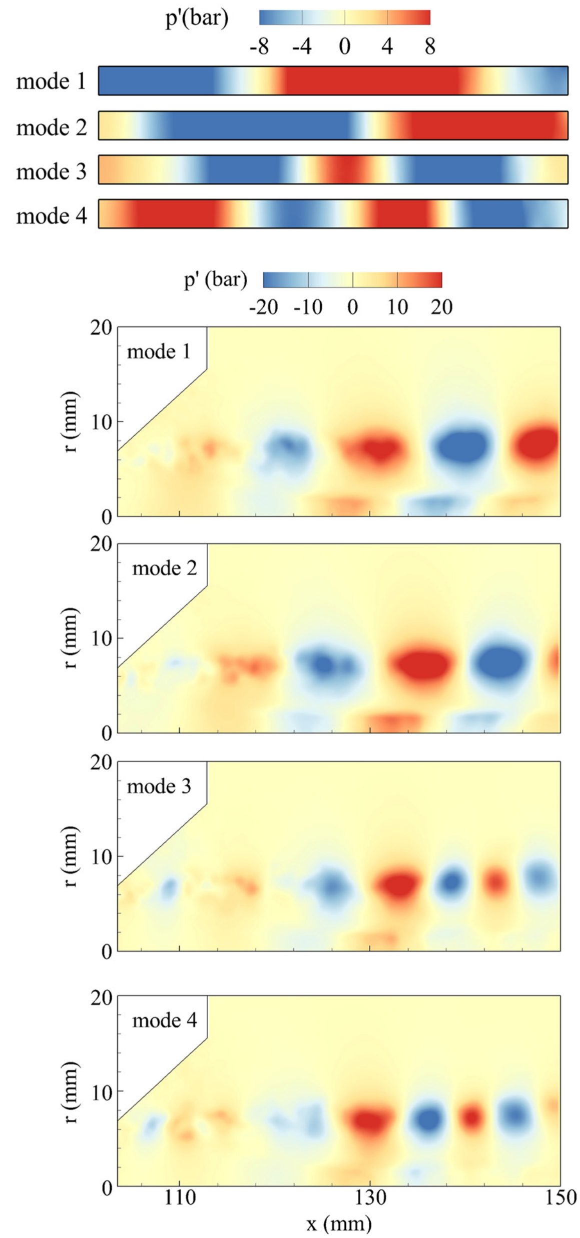

Fig. 12. Distributions of pressure oscillations in the first four POD modes (a) inside GOX post and (b) in the downstream of the taper region for the baseline case.

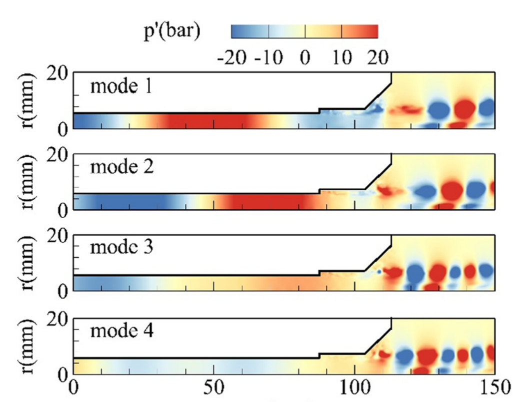

Fig. 13. Distributions of pressure oscillations in the first four POD modes for Case 1.

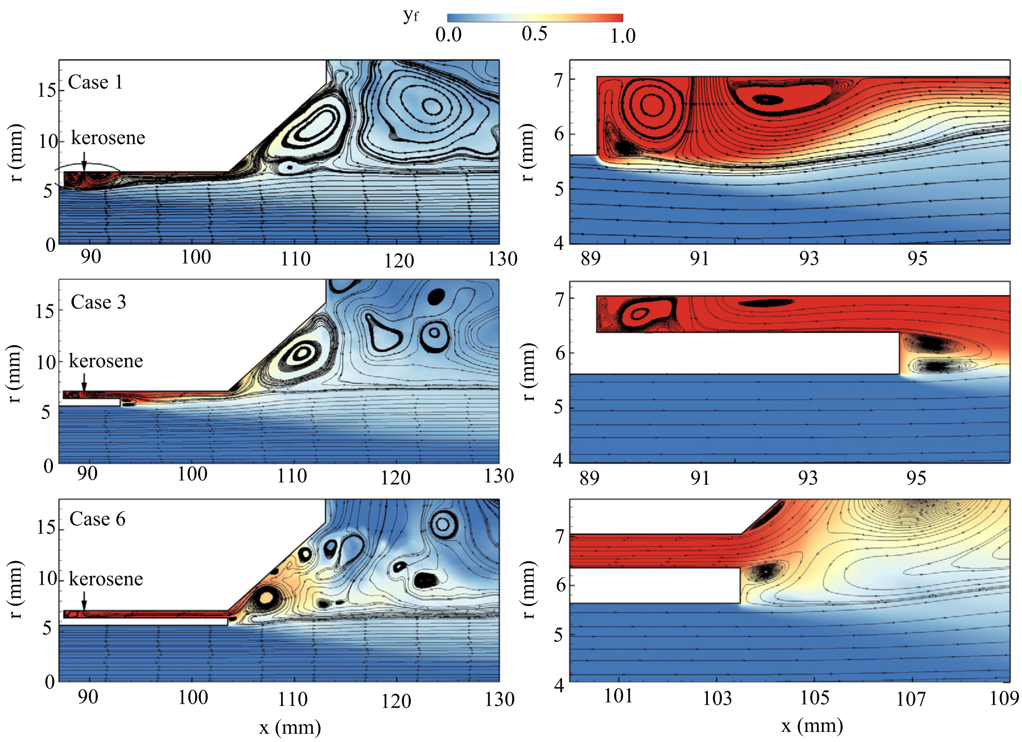

Fig. 14. Global (left) and zoom-in (right) views of time-mean distribution of fuel mass fraction overlaid by streamlines in mixing section of Cases 1, 3 and 6.

(shown over the range of $-20 < p' < 20$ bar in Fig. 12b). Furthermore, the dominant frequencies in the downstream of the taper region are no longer the ones of the longitudinal acoustics. The first two POD modes in Fig. 12b have the dominant frequency of 2.7 kHz, corresponding to vortex shedding. The distance between the centers of two nearby pressure oscillations is $L = 0.008$ m and the velocity of the vortices is $u = 42.5$ m/s, which is estimated as the average of the flows above and below the mixing region. The characteristic frequency of vortex shedding can be estimated as $f = u/2L = 2.7$ kHz. As the recess length decreases, the dominant frequencies after the taper region increase because of the larger velocities of the vortices.

For Case 1, Fig. 13 shows the distributions of pressure oscillations for the first four POD modes over the entire injector. Clear structures are observed at the dominant frequency of 2.7 kHz. The longitudinal acoustic oscillation in the GOX post and Kelvin-Helmholtz instability in the taper and downstream regions "resonates" at one dominant frequency. POD analyses were also performed in individual regions to eliminate uncertainties and similar observations were obtained.

4.3. Mixing characteristics

The mixing between the kerosene and GOX streams is of great concern in the development of a high-performance injector. Fig. 14 shows the time-mean distributions of fuel mass fraction overlaid by streamlines in global and zoom-in views for Cases 1, 3, and 6. Significant differences of near-field flow structures are observed among these cases. For Case 1, without shielding, kerosene is injected directly into the GOX flow. Upstream of the injection slit, kerosene accumulates and rotates in the clockwise direction. The flow structure resembles the combination of a backward-facing step flow and a swirling transverse jet in a crossflow. A thick liquid film is formed downstream the collar rim. For Case 3, with a partial shielding, the protrusion of the GOX post prevents direct injection of kerosene into the GOX flow. Part of the radial momentum in the kerosene stream converts to axial momentum

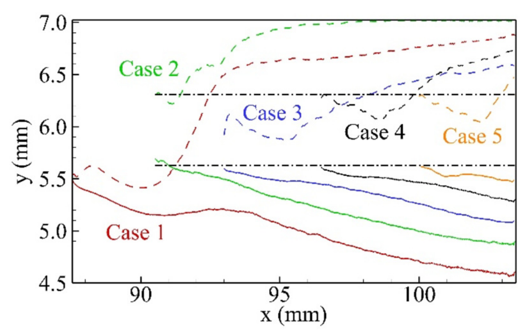

Fig. 15. Spatial location of kerosene mass fractions of 0.1 (solid lines) and 0.9 (dash lines) for Cases 1-5.

in the fuel passage before mixing with GOX, leading to a thinner initial liquid film than that in Case 1. Meanwhile, flow expansion behind the GOX post generates two counter-rotating recirculation bubbles and influences the early development of the mixing layer in the wake of the GOX post. In Cases 1 and 3, both liquid films are gradually entrained by GOX as they evolve in the recess region. For Case 6 with a full shielding, the GOX separates from the kerosene stream and the mixing layer only starts in the diverging section of the injector, prohibiting efficient mixing. Two weak counter-rotating recirculation bubbles occur behind the GOX post, followed by complicated vortical structures in the taper region. In all these cases, a large recirculation zone is observed near the taper wall.

Fig. 15 shows the spatial locations of kerosene mass fractions of 0.1 (solid lines) and 0.9 (dashed lines) for Cases 1-5. The radial extends of the fuel shielding collars are marked by two horizontal dash-dot lines. Since mixing of kerosene and GOX only begins near the post rim, the isolines of kerosene mass faction start at different axial locations. In general, a longer recess length leads to a broader dispersion of kerosene, suggesting a better mixing efficiency. This phenomenon may be attributed to the increased momentum loss in the fuel annulus with longer shielding collars and the shortened development of the mixing layer in the recess region. Among the cases with a partial shielding, Case 2 exhibits the best mixing efficiency. It is worth noting that in the case of combustion the exposure of the injector wall to high-temperature mixture aggravates the thermal loading of the wall, as manifested by Wang et al. [31]. In the worst-case scenario, the injector hardware burns out and causes the failure of an entire engine. The recess length of a GCLSC injector must be carefully chosen to achieve design optimization of mixing efficiency and thermal protection of the injector.

5. Conclusions

The effects of recess length on the flow dynamics and mixing characteristics in gas-centered, liquid-swirl coaxial (GCLSC) injectors are investigated using the large eddy simulation technique. Gaseous oxygen (GOX) is directed axially into the center post at a temperature of 687.7 K, and kerosene is introduced tangentially into the coaxial annulus at a temperature of 492.2 K. The operating pressure is 25.3 MPa, substantially above the thermodynamic pressures of oxygen and kerosene, rendering the flow condition in the supercritical regime.

The flow structures and associated key mechanisms are identified and analyzed. In the recess region, entrainment of low-speed, high-density kerosene to high-speed, low-density GOX induces shear layer instabilities in both the axial and azimuthal directions. The characteristic frequencies of different instability modes are analyzed and matched with empirical correlations. Dynamic analyses are conducted using the power-spectral-density and proper-orthogonal-decomposition methods. Compared to Cases 2-6 with a finite fuel shielding, Case 1 with no shielding has stronger pressure oscillations over the entire injector, which are closely related to the longitudinal acoustic oscillations in the GOX post. The momentum and mass transfer between GOX and kerosene streams at different recess lengths are also examined. The mixing layer expands radially as the flow convects downstream. The influence of recess length on mixing efficiency is quantified and elaborated. Among cases with relatively low-pressure oscillations, Case 2 is found to have the optimal fuel shielding with the best mixing efficiency, while Case 6 with no recess leads to the least efficient mixing due to outward spreading of swirling kerosene at the injector exit.

Declaration of competing interest

The authors declare that they have no known competing financial interests or personal relationships that could have appeared to influence the work reported in this paper.

Data availability

Data will be made available on request.

Acknowledgements

This work was sponsored partly by the Air Force Office of Scientific Research under Grant No. FA9550-18-1-0216, and partly by the William R. T. Oakes Endowment of the Georgia Institute of Technology. The authors gratefully acknowledge support and advice from Dr. Mitat A. Birkan.

References

[1] A. Lefebvre, Atomization and Sprays, vol. 1040, CRC Press, 1988, p. 2756.
[2] V. Yang, M. Habiballah, J. Hulka, M. Popp, Liquid Rocket Thrust Chambers: Aspects of Modeling, Analysis, and Design, vol. 200, AIAA, 2004.
[3] T.C. Lieuwen, V. Yang, Combustion Instabilities in Gas Turbine Engines, vol. 210, AIAA, 2005.
[4] Y. Huang, V. Yang, Dynamics and stability of lean-premixed swirl-stabilized combustion, Prog. Energy Combust. Sci. 35 (2009) 293.
[5] V.G. Bazarov, V. Yang, Liquid-propellant rocket engine injector dynamics, J. Propuls. Power 14 (1998) 797.
[6] V. Bazarov, V. Yang, P. Puri, Design and dynamics of jet and swirl injectors, in: Liquid Rocket Thrust Chambers: Aspects of Modeling, Analysis, and Design, in: Progress in Astronautics and Aeronautics, vol. 200, 2004, p. 19.
[7] A.A. Vasin, S.D. Kamensky, B.I. Katorgin, A.I. Kolesnikov, V.P. Nosov, A.I. Stavrulov, V.V. Fedorov, V.K. Chvanov, Liquid-propellant rocket engine chamber and its casing, U.S. patent US6,244,041 B1, 2001.
[8] M.L. Dranovsky, V. Yang, F. Culick, D.G. Talley, Combustion Instabilities in Liquid Rocket Engines: Testing and Development Practices in Russia, vol. 221, AIAA, 2007.
[9] V. Yang, D.D. Ku, M.L.R. Walker, L.T. Williams, J.C. Leahy, Liquid Oxygen/Kerosene Staged Combustion Rocket Engines with Oxidizer-Rich Preburners, NASA/TP 2015–218203, 2015.
[10] V. Yang, D.D. Ku, C.B. Lioi, S.-T. Yeh, J.C. Leahy, R.J. Kenny, Liquid Oxygen/Kerosene Oxygen-Rich, Staged Combustion Engine Technology Development, NASA/TP 2016–218226, 2016.
[11] C. Lioi, D. Ku, V. Yang, Linear acoustic analysis of main combustion chamber of an oxidizer-rich staged combustion engine, J. Propuls. Power 34 (2018) 1505.
[12] M. Lightfoot, S. Danczyk, D. Talley, A method to predict atomization performance in gas-centered swirl-coaxial injectors, Report AFRL-PR-ED-TP-2007-125, 2007.
[13] S.A. Schumaker, S.A. Danczyk, M.D. Lightfoot, Effect of Cup Length on Film Profiles in Gas-Centered Swirl-Coaxial Injectors, AIAA Paper 2010-368, 2010.
[14] S.A. Schumaker, S.A. Danczyk, M. Lightfoot, Effect of swirl on gas-centered swirl-coaxial injectors, AIAA Paper 2011-5621, 2011.
[15] V. Kulkarni, D. Sivakumar, C. Oommen, T. Tharakan, Liquid sheet breakup in gas-centered swirl coaxial atomizers, J. Fluids Eng. 132 (2010) 011303.
[16] G. Park, J. Lee, I. Lee, Y. Yoon, C.H. Sohn, Geometric effect on spray characteristics of gas-centered swirl coaxial injectors: recess ratio and gap thickness, At. Sprays 27 (2017) 7.
[17] J.-P. Matas, M. Hong, A. Cartellier, Stability of a swirled liquid film entrained by a fast gas stream, Phys. Fluids 26 (2014) 042108.
[18] V. Yang, Modeling of supercritical vaporization, mixing, and combustion processes in liquid-fueled propulsion systems, Proc. Combust. Inst. 28 (2000) 925.
[19] J.G. Kim, Y.M. Han, H.S. Choi, Y. Yoon, Study on spray patterns of gas-centered swirl coaxial (GCSC) injectors in high pressure conditions, Aerosp. Sci. Technol. 27 (2013) 171.
[20] S. Soller, R. Wagner, H. Kau, P. Martin, C. Mäding, Combustion stability characteristics of coax-swirl-injectors for oxygen/kerosene, AIAA Paper 2007-5563, 2007.
[21] M.J. Bedard, B.J. Austin, W.E. Anderson, Detailed Measurement of ORSC Main Chamber Injector Dynamics in a Model Rocket Combustor, AIAA Paper 2018-1186, 2018.
[22] D. Manski, C. Goertz, H.-D. Sabnick, J.R. Hulka, B.D. Goracke, D.J.H. Levack, Cycles for Earth-to-orbit propulsion, J. Propuls. Power 14 (1998) 588.
[23] G. Batchelor, A.E. Gill, Analysis of the stability of axisymmetric jets, J. Fluid Mech. 14 (1962) 529.
[24] K. Ahn, Y.-M. Han, S. Seo, H.-S. Choi, Effects of injector recess and chamber pressure on combustion characteristics of liquid–liquid swirl coaxial injectors, Combust. Sci. Technol. 183 (2010) 252.
[25] K. Ahn, Y.-M. Han, H.-S. Choi, Effects of recess length on discharge coefficients of swirl coaxial injectors, Combust. Sci. Technol. 184 (2012) 323.
[26] X. Wang, Y. Wang, V. Yang, Geometric effects on liquid oxygen/kerosene bi-swirl injector flow dynamics at supercritical conditions, AIAA J. 55 (2017) 3467.
[27] X. Wang, Y. Li, Y. Wang, V. Yang, Near-field flame dynamics of liquid oxygen/kerosene bi-swirl injectors at supercritical conditions, Combust. Flame 190 (2018) 1.
[28] M.P. Juniper, S.M. Candel, The stability of ducted compound flows and consequences for the geometry of coaxial injectors, J. Fluid Mech. 482 (2003) 257.
[29] H.C. Balance, O. Bibik, T.S. Cook, S. Danczyk, S.A. Schumaker, V. Yang, T.C. Lieuwen, Optical diagnostics in a high-pressure combustor with gaseous oxygen and kerosene, J. Propuls. Power 1 (2018) 13.
[30] L. Zhang, X. Wang, Y. Li, S.-T. Yeh, V. Yang, Supercritical fluid flow dynamics and mixing in gas-centered liquid-swirl coaxial injectors, Phys. Fluids 30 (2018) 075106.
[31] X. Wang, L. Zhang, Y. Li, S.-T. Yeh, V. Yang, Supercritical combustion of gas-centered liquid-swirl coaxial injectors for staged-combustion engines, Combust. Flame 197 (2018) 204.
[32] X. Wang, Y. Wang, V. Yang, Three-dimensional flow dynamics and mixing in a gas-centered liquid-swirl coaxial injector at supercritical pressure, Phys. Fluids 31 (2019) 065109.
[33] J.C. Oefelein, V. Yang, Modeling high-pressure mixing and combustion processes in liquid rocket engines, J. Propuls. Power 14 (1998) 843.
[34] H. Meng, V. Yang, A unified treatment of general fluid thermodynamics and its application to a preconditioning scheme, J. Comput. Phys. 189 (2003) 277.
[35] X. Wang, H. Huo, U. Unnikrishnan, V. Yang, A systematic approach to high-fidelity modeling and efficient simulation of supercritical fluid mixing and combustion, Combust. Flame 195 (2018) 203.

[36] G. Erlebacher, M. Hussaini, C. Speziale, T.A. Zang, Toward the large-eddy simulation of compressible turbulent flows, J. Fluid Mech. 238 (1992) 155.
[37] P. Dagaut, On the kinetics of hydrocarbons oxidation from natural gas to kerosene and diesel fuel, Phys. Chem. Chem. Phys. 4 (2002) 2079.
[38] S.-Y. Hsieh, V. Yang, A preconditioned flux-differencing scheme for chemically reacting flows at all Mach numbers, Int. J. Comput. Fluid Dyn. 8 (1997) 31.
[39] N. Zong, V. Yang, An efficient preconditioning scheme for real-fluid mixtures using primitive pressure–temperature variables, Int. J. Comput. Fluid Dyn. 21 (2007) 217.
[40] H.-G. Li, N. Zong, X.-Y. Lu, V. Yang, A consistent characteristic boundary condition for general fluid mixture and its implementation in a preconditioning scheme, Adv. Appl. Math. Mech. 4 (2012) 72.
[41] D.J. Bodony, Analysis of sponge zones for computational fluid mechanics, J. Comput. Phys. 212 (2006) 681.
[42] L. Zhang, V. Yang, Flow dynamics and mixing of a transverse jet in crossflow—Part I: steady crossflow, J. Eng. Gas Turbines Power 139 (2017) 082601.
[43] X. Wang, H. Huo, Y. Wang, V. Yang, Comprehensive study of cryogenic fluid dynamics of swirl injectors at supercritical conditions, AIAA J. 55 (2017) 9.
[44] N. Zong, V. Yang, Cryogenic fluid dynamics of pressure swirl injectors at supercritical conditions, Phys. Fluids 20 (2008) 056103.
[45] X. Chen, V. Yang, Effect of ambient pressure on liquid swirl injector flow dynamics, Phys. Fluids 26 (2014) 102104.
[46] N. Zong, V. Yang, Cryogenic fluid jets and mixing layers in transcritical and supercritical environments, Combust. Sci. Technol. 178 (2006) 1–3.
[47] N. Trask, D. Schmidt, M. Lightfoot, S. Danczyk, Compressible modeling of the internal two-phase flow in a gas-centered swirl coaxial fuel injector, J. Propuls. Power 28 (2012) 4.
[48] J. Panda, D. McLaughlin, Experiments on the instabilities of a swirling jet, Phys. Fluids 6 (1994) 263.
[49] X. Lu, S. Wang, H.-G. Sung, S.-Y. Hsieh, V. Yang, Large-eddy simulations of turbulent swirling flows injected into a dump chamber, J. Fluid Mech. 527 (2005) 171.
[50] C.-M. Ho, P. Huerre, Perturbed free shear layers, Annu. Rev. Fluid Mech. 16 (1984) 365.